CAMBRIDGE
UNIVERSITY PRESS

Research Article

The MAGPI Survey: Insights into the Lyα line widths and the size of ionised bubbles at the edge of cosmic reionisation

Tamal Mukherjee[1,2,3], Tayyaba Zafar[1,2,3], Themiya Nanayakkara[2,4], Anshu Gupta[2,5], Siddhartha Gurung-López[6,7], Andrew Battisti[2,8,10], Emily Wisnioski[2,8], Caroline Foster[2,9], Jon Trevor Mendel[2,8], Katherine Harborne[2,10], Claudia Lagos[2,10], Tadayuki Kodama[11], Scott Croom[2,12], Sabine Thater[13], Jacinda Webb[1,3], Stefania Barsanti[8,12], Sarah Sweet[2,14], Jahang Prathap[1,2,3], Lucas Valenzuela[15], Anilkumar Mailvaganam[1,2,3] and Jose Luis Carrillo Martinez[1,2,3]

[1]School of Mathematical and Physical Sciences, Macquarie University, Sydney, NSW, Australia, [2]ARC Centre of Excellence for All Sky Astrophysics in 3 Dimensions (ASTRO 3D), Canberra, Australia, [3]Astrophysics and Space Technologies Research Centre, Macquarie University, Sydney, NSW, Australia, [4]Centre for Astrophysics and Supercomputing, Swinburne University of Technology, Hawthorn, VIC, Australia, [5]International Centre for Radio Astronomy Research (ICRAR), Curtin University, Bentley, WA, Australia, [6]Observatori Astronòmic de la Universitat de València, Ed. Instituts d'Investigació, Paterna, Valencia, Spain, [7]Departament d'Astronomia i Astrofísica, Universitat de València, Burjassot, Spain, [8]Research School of Astronomy and Astrophysics, Australian National University, Canberra, ACT, Australia, [9]School of Physics, University of New South Wales, Sydney, NSW, Australia, [10]International Centre for Radio Astronomy Research (ICRAR), The University of Western Australia, Crawley, WA, Australia, [11]Astronomical Institute, Tohoku University, Sendai, Japan, [12]Sydney Institute for Astronomy, School of Physics, University of Sydney, Sydney, NSW, Australia, [13]Department of Astrophysics, University of Vienna, Vienna, Austria, [14]School of Mathematics and Physics, University of Queensland, Brisbane, QLD, Australia and [15]Universitäts-Sternwarte, Fakultät für Physik, Ludwig-Maximilians-Universität München, Munich, Germany

Abstract

We present spectroscopic properties of 22 Lyα emitters (LAEs) at $z = 5.5 - 6.6$ with Lyα luminosity $\log(L_{\text{Ly}\alpha} \, [\text{erg s}^{-1}]) = 42.4 - 43.5$, obtained using VLT/MUSE as part of the Middle Ages Galaxy Properties with Integral Field Spectroscopy (MAGPI) survey. Additionally, we incorporate broad-band photometric data from the Subaru Hyper Suprime-Cam (HSC) Wide layer for 17 LAEs in our sample. The HSC-y band magnitudes show that our LAEs are UV-bright, with rest-frame absolute UV magnitudes $-19.74 \leq M_{\text{UV}} \leq -23.27$. We find that the Lyα line width increases with Lyα luminosity, and this trend becomes more prominent at $z > 6$ where Lyα lines become significantly broadened ($\gtrsim +260$ km s^{-1}) at luminosities $\log(L_{\text{Ly}\alpha} \, [\text{erg s}^{-1}]) > 43$. This broadening is consistent with previous studies, suggesting that these sources are located inside larger ionised bubbles. We observe a slightly elevated ionising photon production efficiency estimated for LAEs at $z > 6$, which indicates that younger galaxies could be producing more ionising photons per UV luminosity. A tentative anti-correlation between ionising photon production efficiency and Lyα rest-frame equivalent width is noticed, which could indicate a time delay between production and escape of ionising photon primarily due to supernovae activity. Furthermore, we find a positive correlation between radius of ionised regions and Lyα line width, which again suggests that large ionised bubbles are created around these LAEs, which are allowing them to self-shield from the scattering effects of the intergalactic medium (IGM). We also detect two very closely separated LAEs at $z = 6.046$ (projected spatial distance between the cores is 15.92 kpc). This is the LAE pair with the smallest separation ever discovered in the reionisation epoch. The size of their respective bubbles suggests that they likely sit inside a common large ionised region. Such a closely separated LAE pair increases the size of ionised bubble, potentially allowing a boosted transmission of Lyα through neutral IGM and also supports an accelerated reionisation scenario.

Keywords: Cosmology: dark ages; reionisation; first stars – galaxies: evolution; high redshift; intergalactic medium

1. Introduction

Cosmic reionisation, a pivotal epoch in the history of the Universe, marks the last phase transition of the Universe when neutral

hydrogen (H I) in the intergalactic medium (IGM) became fully ionised, ending the cosmic 'Dark Ages.' However, the precise timing of reionisation and sources capable of emitting sufficient ionising photons remain subjects of active debate till date. Previously, it was believed that reionisation was largely complete by $z \sim 6$ (Fan et al. 2006). However, recent studies suggest a relatively late end of reionisation at $z \sim 5.3 - 5.5$ (Becker et al. 2015; Kulkarni et al. 2019; Cain et al. 2021; Bosman et al. 2022). A common belief is that galaxies which are faint in intrinsic ultraviolet (UV) radiation are the primary contributors of reionisation, typically releasing about 10 % of their Lyman continuum (LyC) photons (see Finkelstein

et al. 2019; Dayal et al. 2020). However, to explain the relatively rapid decrease in the neutral IGM fraction in later epochs, it is possible that more infrequent luminous sources might also have played a significant role (see Naidu et al. 2020).

Due to the attenuation of UV photons below the Lyman break by the increasingly neutral IGM at $z > 4$ (e.g. Inoue et al. 2014; Steidel et al. 2018), direct observation of LyC photons is almost impossible. Reionisation models suggest that a minimum escape fraction of LyC photons, $f_{esc}^{LyC} \gtrsim 10\%$ is required to complete reionisation (Robertson et al. 2015; Finkelstein et al. 2019). Therefore, it is crucial to comprehend how LyC photons escape into the IGM and subsequently ionise it during the epoch of reionisation (EoR). Several studies have attempted to make connection between f_{esc}^{LyC} and nebular emission line features such as [O III], C IV, C III Mg II etc (see, Izotov et al. 2020; Nakajima et al. 2020; Schaerer et al. 2022; Katz et al. 2022; Xu et al. 2022; Mascia et al. 2023; Choustikov et al. 2024).

The Lyα emission line of atomic hydrogen has been identified as the most reliable indirect tracer of LyC leakage and is used as one of the promising probes of the EoR (Kakiichi et al. 2016; Laursen et al. 2019; Tang et al. 2023). A rapid decline in the fraction of Lyα emitting galaxies (LAEs) towards higher redshifts ($z > 5$) has been interpreted as a rapid escalation in the H I fraction with increasing redshift (Pentericci et al. 2011; Tilvi et al. 2014; Stark et al. 2017; Hoag et al. 2019; Whitler et al. 2020; Jones et al. 2024; Nakane et al. 2024; Napolitano et al. 2024; Tang et al. 2024a). Both the observed intensity and shape of the Lyα line offer delicate insights into the proportion of H I within the IGM (Robertson et al. 2010). The Lyα rest-frame equivalent width (EW_0) has been identified as an excellent indicator of Lyα escape fraction ($f_{esc}^{Ly\alpha}$; see Matthee et al. 2017b; Begley et al. 2024; Tang et al. 2024b). The separation between the blue and red peaks in the double-peak emission can be used to infer H I column densities (N_{HI}), consequently, the escape of LyC photons (see, Verhamme et al. 2015; Verhamme et al. 2017; Izotov et al. 2018; Naidu et al. 2022). Furthermore, the detection of a stronger blue-peak profile also indicates a very low column density channel of H I that can leak LyC photons (see, Furtak et al. 2022; Mukherjee et al. 2023). However, the blue-peak is expected to be scattered away by the neutral IGM at $z > 5$ (Hu et al. 2010; Hayes et al. 2021), leaving only a single-peak red-skewed profile.

Narrow-band (NB) surveys have discovered a substantial sample of LAE at $z = 5.7$ and $z = 6.6$ (see Hu et al. 2010; Matthee et al. 2015; Santos, Sobral, & Matthee 2016; Bagley et al. 2017; Konno et al. 2018; Taylor et al. 2020; Taylor et al. 2021), and several LAE have also been detected at $z = 6.9$ (Hu et al. 2017) and $z = 7.3$ (Konno et al. 2014). Recent data from the James Webb Space Telescope (JWST) has also contributed to the unprecedented characterisation of LAEs throughout the EoR (Tang et al. 2023; Jung et al. 2024; Witten et al. 2024). The advent of giant imagers, such as Subaru/ Hyper Suprime-Cam (HSC; Miyazaki et al. 2018), has allowed detections of several rare ultra-luminous LAEs (ULLAEs) with $\log(L_{Ly\alpha} \ [erg \ s^{-1}]) > 43.5$ (see, Songaila et al. 2022), including the detections of extremely rare double-peaked LAEs with a blue-wing (see Hu et al. 2016; Songaila et al. 2018; Meyer et al. 2021).

The Multi Unit Spectroscopic Explorer (see, Bacon et al. 2010) on the Very Large Telescope (VLT) has been instrumental in identifying faint LAEs during the EoR (up to $z \sim 6.6$) by pro-

viding deep, high-resolution spectral data across a wide field of view, without any redshift restrictions of NB imaging (see, Hashimoto et al. 2017; Urrutia et al. 2019; Kerutt et al. 2022; Bacon et al. 2023).

Reionisation is known to be an inhomogeneous process (Pentericci et al. 2014; Becker et al. 2015; Bosman et al. 2022), indicating that galaxies in denser regions are likely to create the first 'ionised bubbles' in the Universe (Mason et al. 2018; Endsley et al. 2021a; Jung et al. 2022b; Endsley & Stark 2022; Whitler et al. 2024), which then preferentially emit Lyα radiation once they reach a significant size. As a result, the most distant LAEs are vital for observing and mapping the reionisation process. Strong Lyα emission at $z \gtrsim 6$ often indicates the presence of large ionised bubbles in an otherwise neutral IGM, providing direct observational insights into the reionised regions of the early Universe. When Lyα photons are emitted from galaxies located within large ionised bubbles, they undergo cosmological redshifting far into the damping wing before encountering neutral hydrogen. As a result, they transmit more effectively through IGM (Weinberger et al. 2018; Mason & Gronke 2020; Smith et al. 2022; Qin et al. 2022). Recent studies have found that Lyα line width increases with luminosity and this trend becomes more prominent at $z = 6.6$ (see, Matthee et al. 2017b; Songaila et al. 2024), where higher-luminosity LAEs with $\log(L_{Ly\alpha} \ [erg \ s^{-1}]) \gtrsim 43.25$ show significantly broad Lyα lines (Songaila et al. 2024). At higher redshifts, the IGM becomes more neutral, increasing Lyα line scattering and hence narrowing of the lines is expected. The lack of this effect in brighter LAEs suggests that they reside in more ionised regions, shielding themselves from scattering.

One of the key components in determining the ionising photon budget is the ionising photon production efficiency (ξ_{ion}), which is defined as the ratio between the production rate of ionising photons over the non-ionising UV luminosity density. It has been found that as we delve deeper into the universe's history, young galaxies seem to appear more efficient in producing ionising photons (see, Bouwens et al. 2016; Endsley et al. 2021b; Prieto-Lyon et al. 2023; Simmonds et al. 2023; Tang et al. 2023). Moreover, UV-faint galaxies with Lyα emission are found to have enhanced ξ_{ion} (Maseda et al. 2020; Ning et al. 2023; Saxena et al. 2024; Lin et al. 2024) at $z \sim 6$, making LAEs in the reionisation era the most exciting sources for studying and constraining reionisation.

In this paper, we present spectroscopic properties of 22 new LAEs at the end of reionisation ($z = 5.5 - 6.6$) found in the MUSE data obtained as a part of the Middle Ages Galaxy Properties with Integral Field Spectroscopy (MAGPI) survey (Foster et al. 2021). We restrict this current study to redshifts of $z \gtrsim 5.5$, considering the global neutral hydrogen fraction approaches $x_{HI} \sim 0$ at around $z \sim 5.5$ in 'late' reionisation scenarios (Kulkarni et al. 2019; Bosman et al. 2022). We constrain the evolution of Lyα line width as a function of Lyα luminosity up to $z \sim 7$. Using spectroscopic information of these LAEs, along with the Subaru Hyper-Suprime Cam (HSC) optical photometric information, we estimate their ionising photon contribution toward the global reionisation budget. We also estimate the size of ionised bubbles around these LAEs to investigate the mechanism leading to the visibility of strong Lyα emission even beyond $z > 6$.

The layout of this paper is as follows: In Section 2, we describe the reduction and selection of MUSE data of

potential LAE candidates along with the extraction of HSC photometric magnitudes. Section 3 explores the data analyses: Lyα line fitting and spectroscopic and photometric measurements. Section 4 presents results on the evolution of the Lyα line widths and give an insight into the potential ionised bubbles surrounding these LAEs and also discusses these findings in context of previous works. The main conclusions and summary of this study are presented in Section 5. Throughout this paper, we assume a standard flat ΛCDM cosmology with parameters $H_0 = 70$ km s^{-1}Mpc^{-1}, $\Omega_m = 0.3$, and $\Omega_\Lambda = 0.7$.

2. Observations and data

2.1 MUSE spectroscopic data

The MAGPI survey[a] is an ongoing Large Program on the VLT/MUSE, targeting 56 fields from the Galaxy and Mass Assembly (GAMA; Driver et al. 2011) G12, G15, and G23 fields. MAGPI also includes archival observations of legacy fields Abell 370 and Abell 2744. The survey targets a total of 60 primary galaxies with stellar masses $M_* > 7 \times 10^{10}$ M$_\odot$ and ~100 satellite galaxies with $M_* > 10^9$ M$_\odot$. The primary objective of MAGPI is to conduct a detailed spatially resolved spectroscopic analysis of stars and ionised gas within $0.25 < z < 0.35$ galaxies (see Foster et al. 2021). Data are taken using the MUSE Wide Field Mode ($1' \times 1'$) with a spatial sampling rate of $0.2''$/pixel and the median Full Width at Half Maximum (FWHM) is $0.64''$ in g band, $0.6''$ in r band and $0.55''$ in i band. Each field is observed in six observing blocks, each comprising $2 \times 1\,320$ s exposures, resulting in a total integration time of 4.4 h. The survey primarily employs the nominal mode, providing a wavelength coverage ranging from 4 700 to 9 350 Å, with a dispersion of 1.25 Å. Ground-layer adaptive optics (GLAO) is used to correct atmospheric seeing effects, resulting in a gap between 5 805 and 5 965 Å due to the GALACSI laser notch filter. The depth of MAGPI data allows for the detection of both foreground sources within the Local Universe and distant background sources, including LAEs at $2.9 \lesssim z \lesssim 6.6$.

The raw MUSE data cubes are reduced using `Pymusepipe2`[b], a Python wrapper for the ESO MUSE reduction pipeline (Weilbacher et al. 2020). This pipeline is used to perform the standard bias and overscan subtraction, flat-fielding, wavelength calibration, and telluric correction. Additional information about the data reduction process is provided in Foster et al. (2021) and it will be presented in a greater detail (Mendel et al. in prep.). `LSDCat`[c] (Herenz & Wisotzki 2017) was used for the identification of faint sources – particularly LAEs – accompanied by both automated and visual inspection. LAEs are confirmed using visual inspections of line-profiles and using `MARZ`[d] redshifting software (Hinton et al. 2016) to rule out interlopers. This search led to the detection of 380 new LAEs distributed across 35 MAGPI fields (Mukherjee et al. in preparation). Among these, we found 22 LAEs with log ($L_{Ly\alpha}$ [erg s^{-1}]) > 42.4 at $5.5 \lesssim z \lesssim 6.6$.

Table 1. HSC photometry of MAGPI LAEs at $z = 5.5 - 6.6$, in order of increasing redshift. HSC-i, z and y band AB magnitudes, and 2σ limits (for non-detections) are presented. M$_{UV}$ is the rest-frame absolute UV magnitude estimated from the y-band magnitudes.

MAGPI ID	HSC-i	HSC-z	HSC-y	M$_{UV}$
1507091138	25.52 ± 0.12	25.10 ± 0.18	24.43 ± 0.19	−22.20
1527275156	25.29 ± 0.13	25.34 ± 0.29	24.46 ± 0.21	−22.17
2310233132	−	−	−	−
1527283124	26.21 ± 0.33	26.10 ± 0.45	26.66 ± 1.08	−19.96
1503111271	26.04 ± 0.24	26.86 ± 0.91	25.82 ± 0.86	−20.80
1507313178	> 27.18	> 26.86	> 25.75	> −20.87
1511268137	> 27.55	> 27.49	> 26.21	> −20.41
1207184066	−	−	−	−
2306257117	−	−	−	−
1205187075	> 28.25	> 29	> 26.40	> −20.22
1523134187	25.59 ± 0.19	24.39 ± 0.32	24.31 ± 0.33	−22.30
1507308274	> 29	> 27.37	> 25.19	> −21.42
2310245276	−	−	−	−
1204117107	26.82 ± 0.49	25.26 ± 0.25	24.33 ± 0.19	−22.28
1529110045	25.74 ± 0.13	25.26 ± 0.16	25.60 ± 0.40	−21.01
1529106057	25.93 ± 0.23	24.49 ± 0.16	25.06 ± 0.35	−21.55
2310222098	−	−	−	−
1528094186	26.72 ± 0.42	< 27.61	25.38 ± 0.5	−21.22
1505103163	25.85 ± 0.25	25.84 ± 0.56	23.32 ± 0.30	−23.27
1530068179	> 26.17	> 27	> 26.85	> −19.74
1528263095	> 26.13	> 27.44	> 26.46	> −20.12
1522272275	25.87 ± 0.22	27.05 ± 1.01	25.25 ± 0.41	−21.33

2.2 HSC photometry

We use optical photometric data for 17 MAGPI LAEs of our sample that are covered in the broad-band filters (g, r, i, z and y) of Subaru HSC Wide layer. HSC Strategic Program (see Aihara et al. 2018) is a wide-field optical imaging survey on the 8.2 meter Subaru Telescope. The HSC-Wide layer data cover about 300 deg^2 in all five broad-band filters to the nominal survey exposure (10 min in g and r bands and 20 min in i, z, and y bands; see Aihara et al. 2019) with a median seeing $0.6''$ in the i-band.

Using HSC command-line SQL (Structured Query Language) tool[e], we retrieve the Wide layer photometric data from data-release 2 (Aihara et al. 2019). We extract fluxes and corresponding 1σ flux uncertainties and limiting 2σ fluxes (for non-detections) using $2''$ aperture diameter. These fluxes and corresponding uncertainties for i, z, and y bands are presented in Table 1.

3. Data analyses

For our sample of 22 LAEs, 1D spectra are extracted using an aperture of $2''$ radius. MUSE 1D spectra reveal the detection of Lyα emissions where spectroscopic redshifts are determined based on the peak of the Lyα line. No other associated emission lines are found in the MUSE data for these 22 LAEs, restricting the

measurement of systemic redshift. Below we estimate UV magnitudes and discuss the procedures of analysing Lyα spectra to study properties of these LAEs.

3.1 Estimating UV magnitudes

Out of the 22 sources, 11 LAEs are detected in HSC broad-band filters. HSC does not cover GAMA23 fields and hence we do not have photometric data for four sources in this field. We also do not have photometric data for MAGPI1207184066 as it is located at the edge of the HSC field. For rest of the six sources, which are not detected in HSC, we calculate a $2\,\sigma$ limit on the magnitudes (see Table 1). As we do not have photometry beyond y band, no meaningful constraints can be obtained on the UV slope (β). Therefore, we assume a flat UV slope $\beta = -2$, which is the typical value that most of the high-redshift galaxies have (see, Dunlop et al. 2013; Bouwens et al. 2014; Matthee et al. 2017b). We convert the y band magnitudes to the rest-frame absolute UV magnitudes (M_{UV}) at 1 500 Å. We also note that, for $z > 6$ sources, y-band magnitude is not exactly measuring the flux at 1 500 Å. Still, it provides a decent approximation of the UV magnitudes. The estimated UV magnitudes of our sources lie in the range $-19.74 \lesssim M_{UV} \lesssim -23.27$, which are given in Table 1.

3.2 Line profile fitting

We use `pyplatefit`,[f] a python module (Bacon et al. 2023) to fit a local continuum and obtain a continuum subtracted spectrum. `pyplatefit` performs a continuum fit around the observed Lyα line in a spectral window of ± 50 Å centred on the Lyα line, using a simple stellar population model (Bruzual & Charlot 2003). It then subtracts the continuum and returns a continuum-subtracted spectrum. Next we fit the continuum subtracted Lyα profiles using an asymmetric Gaussian which has been found to provide an extremely good representation of the Lyα line (see Shibuya et al. 2014; Herenz et al. 2017; Claeyssens et al. 2019; Songaila et al. 2024):

$$F(\lambda) = f_{max} \exp\left(-\frac{\Delta v^2}{2(a_{asym}(\Delta v) + w)^2}\right) \quad (1)$$

where f_{max} is the flux normalisation (amplitude), Δv is the velocity shift (in km s^{-1}) relative to the peak velocity, a_{asym} determines the asymmetry or skewness of the line and w (in km s^{-1}) controls the line width (FWHM). A positive asymmetry value suggests that the Lyα line has a red wing, which is usually seen in most of the single-peaked Lyα lines (Kerutt et al. 2022; Songaila et al. 2022). The line width can be obtained in terms of fitting parameters as follows (see also, Claeyssens et al. 2019; Songaila et al. 2024):

$$FWHM\ (km\ s^{-1}) = \frac{2\sqrt{2\ln(2)}\ w}{(1 - 2\ln(2)\ a_{asym}^2)} \quad (2)$$

The corresponding error in the FWHM is almost fully dominated by the error in w, with only a few percent contribution from the asymmetry term. The fits on the continuum-subtracted spectra along with the values of the free parameters and corresponding 1σ errors are shown in Appendix 1.

[f]https://github.com/musevlt/pyplatefit.
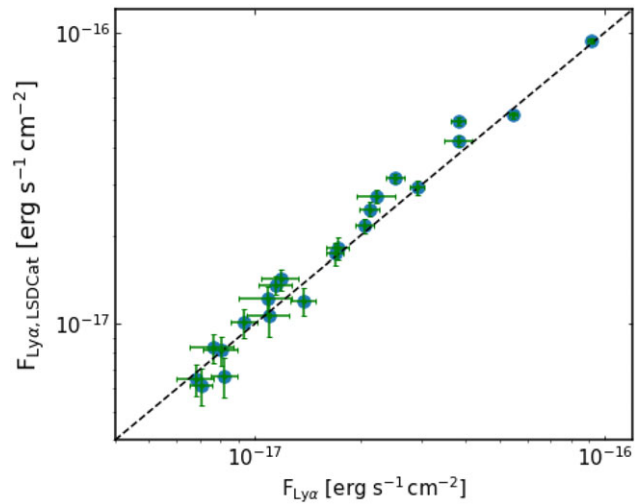
Figure 1. Lyα line fluxes obtained from MUSE 1D spectra (extracted using 2″ radius aperture) are compared against `LSDCat` 3 R_{KRON} fluxes. The one-to-one relation is shown as the dashed line.

3.3 Spectroscopic measurements

Using a single asymmetric Gaussian fit to the Lyα profile extracted using 2″ radius aperture, as mentioned above, we measure Lyα line fluxes ($F_{Ly\alpha}$) for our LAEs. In Fig. 1, we compare them with the 3 R_{KRON} fluxes obtained using `LSDCat` (flux extracted using the aperture of radius $3 \times R_{KRON}$ that contains $> 95\%$ of the total line flux; (see, Graham & Driver 2005; Herenz et al. 2017). The values of 3 R_{KRON} radii in which fluxes were extracted are ranging from 1.6″ to 2.2″. Since both flux values match well, we conclude that our line flux measurements are accurate. The observed Lyα luminosities ($L_{Ly\alpha}$) are then calculated from fluxes as $L_{Ly\alpha} = 4\pi\,F_{Ly\alpha}D_L^2$, where D_L is the luminosity distance, calculated using the cosmological parameters that we assume in Section 1.

We measure the Lyα EW_0 to investigate the strength of the Lyα line. In order to do that, we need measurements of UV continuum flux density at the Lyα wavelength. However, due to lack of UV-slope measurement (see Section 3.1), it is not possible to determine continuum flux density from the photometric data. Further, Hashimoto et al. (2017) caution that fixing the value of UV-slope β at high-redshift can lead to an underestimation of EW_0 due to the redshift evolution of β. Therefore, we obtain the observed median UV-continuum flux density ($f_{Ly\alpha}^{cont}$) from the continuum fit performed using `pyplatefit` (see Section 3.2). We then divide the total Lyα line flux ($F_{Ly\alpha}$) by $f_{Ly\alpha}^{cont}$ to determine observed Lyα equivalent width (EW). The rest-frame equivalent width is then given as $EW_0 = EW/(1 + z)$. We note that for some LAEs, the continuum in the MUSE data is too faint, and thus we can only derive lower limits for EW_0 for them. As Hα emission is not covered within the MUSE spectral range, Lyα escape fraction cannot be directly measured. A strong correlation between $f_{esc}^{Ly\alpha}$ and EW_0 has been found in both low- and high-redshift LAEs (see, Matthee et al. 2017b; Yang et al. 2017; Sobral & Matthee 2019; Begley et al. 2024). In Begley et al. (2024), a sample of 152 star-forming galaxies with $z \sim 4 - 5$ is used to obtain a linear dependence between $f_{esc}^{Ly\alpha}$ and EW_0. We estimate $f_{esc}^{Ly\alpha}$ using this best-fit relation. We tabulate the spectroscopic properties of these LAEs in Table 2.

Table 2. Properties of 22 MAGPI LAEs at $5.5 \lesssim z \lesssim 6.6$ in the sample, in order of increasing redshift. Columns are as follows: MAGPI ID; RA: Right Ascension in degrees; DEC: Declination in degrees; z: Redshift based on the peak of the Lyα line; $\log_{10}(L_{Ly\alpha})$: observed Lyα luminosity in erg s^{-1}; FWHM: Lyα line width measured using asymmetric Gaussian fit; $f_{Ly\alpha}^{cont}$ *: Observed UV-continuum flux-density at the location of Lyα wavelength, in 10^{-20} erg s^{-1}cm^{-2}Å^{-1}; EW$_0$: Spectroscopically measured Lyα rest-frame equivalent width; $f_{esc}^{Ly\alpha}$: Lyα escape fraction; $\log(\xi_{ion})$: Ionising photon production efficiency in Hz erg^{-1}; R_B: radius of bubble ionised by LAE itself, in pMpc.

MAGPI ID	RA (deg)	DEC (deg)	z	$\log_{10}(L_{Ly\alpha})$ (erg s^{-1})	FWHM (km s^{-1})	$f_{Ly\alpha}^{cont}$ *	EW$_0$ (Å)	$f_{esc}^{Ly\alpha}$	$\log(\xi_{ion})$ (Hz erg^{-1})	R_B (pMpc)
1507091138	215.6265	0.4041	5.4955	42.77 ± 0.04	235.45 ± 24.65	12.09	23.18 ± 3.28	$0.087^{+0.019}_{-0.017}$	25.26 ± 0.03	0.55 ± 0.02
1527275156	220.0398	-0.6588	5.5010	43.50 ± 0.01	274.29 ± 8.56	19.89	72.24 ± 9.65	$0.273^{+0.060}_{-0.054}$	25.51 ± 0.01	0.66 ± 0.04
2310233132	348.3007	-34.0181	5.5267	42.76 ± 0.03	240.43 ± 15.01	4.05	66.27 ± 12.43	$0.251^{+0.070}_{-0.062}$	$-$	0.38 ± 0.03
1527283124	220.0399	-0.6613	5.5393	42.98 ± 0.04	211.52 ± 17.15	6.28	70.2 ± 17.91	$0.266^{+0.094}_{-0.083}$	25.88 ± 0.34	0.44 ± 0.05
1503111271	213.6237	-0.4111	5.6483	42.97 ± 0.03	252.83 ± 27.29	20.88	19.74 ± 4.71	$0.074^{+0.024}_{-0.021}$	26.08 ± 0.26	0.65 ± 0.07
1507313178	215.6141	0.4064	5.6570	42.87 ± 0.03	272.68 ± 15.15	9.45	34.50 ± 7.16	$0.130^{+0.039}_{-0.034}$	< 25.72	0.51 ± 0.04
1511268137	216.5675	1.7274	5.7198	42.55 ± 0.05	175.55 ± 17.04	2.17	69.01 ± 37.78	$0.261^{+0.175}_{-0.152}$	< 25.28	0.31 ± 0.09
1207184066	182.0006	-2.4909	5.7643	42.40 ± 0.04	295.35 ± 32.29	3.27	29.36 ± 8.73	$0.110^{+0.043}_{-0.038}$	$-$	0.37 ± 0.04
2306257117	345.0617	-34.4722	5.7750	42.40 ± 0.06	213.43 ± 17.21	4.09	25.40 ± 8.09	$0.095^{+0.040}_{-0.035}$	$-$	0.38 ± 0.05
1205187075	178.0804	-0.8336	5.8010	42.47 ± 0.05	266.47 ± 46.14	3.22	37.10 ± 15.06	$0.140^{+0.074}_{-0.065}$	< 25.54	0.36 ± 0.06
1523134187	219.5444	-1.0999	5.9285	42.65 ± 0.03	237.48 ± 34.83	3.77	42.10 ± 14.68	$0.158^{+0.072}_{-0.063}$	24.84 ± 0.01	0.39 ± 0.06
1507308274	215.6144	0.4117	5.9815	42.73 ± 0.03	256.93 ± 33.13	19.36	10.06 ± 1.59	$0.037^{+0.008}_{-0.007}$	< 25.90	0.66 ± 0.03
2310245276	348.2999	-34.0101	6.0390	42.52 ± 0.04	199.64 ± 20.64	4.96	23.54 ± 6.15	$0.088^{+0.031}_{-0.027}$	$-$	0.39 ± 0.07
1204117107	175.6656	-0.79936	6.0460	43.18 ± 0.02	367.48 ± 25.83	35.76	12.50 ± 3.15	$0.046^{+0.016}_{-0.014}$	25.91 ± 0.03	0.86 ± 0.09
1529110045	220.3717	-0.1079	6.0462	42.93 ± 0.03	197.49 ± 18.16	8.11	43.2 ± 13.37	$0.163^{+0.067}_{-0.059}$	25.62 ± 0.06	0.47 ± 0.06
1529106057	220.3720	-0.1072	6.0464	43.27 ± 0.01	262.15 ± 21.19	18.08	38.92 ± 7.83	$0.147^{+0.043}_{-0.038}$	25.79 ± 0.04	0.63 ± 0.06
2310222098	348.3013	-34.0200	6.1485	43.40 ± 0.01	329.61 ± 20.75	11.07	65.81 ± 9.58	$0.241^{+0.057}_{-0.052}$	$-$	0.59 ± 0.05
1528094186	219.5400	-1.1004	6.1662	42.78 ± 0.04	230.72 ± 26.26	15.77	12.65 ± 4.23	$0.047^{+0.020}_{-0.018}$	25.83 ± 0.18	0.57 ± 0.05
1505103163	214.6632	-1.7198	6.2481	42.72 ± 0.05	221.43 ± 47.02	12.26	13.73 ± 2.55	$0.051^{+0.014}_{-0.012}$	25.01 ± 0.01	0.57 ± 0.03
1530068179	222.1510	2.9404	6.4202	42.80 ± 0.04	247.26 ± 20.11	4.97	37.43 ± 12.97	$0.141^{+0.063}_{-0.056}$	< 26.06	0.42 ± 0.06
1528263095	220.2286	-1.6538	6.5540	42.57 ± 0.06	163.44 ± 21.19	6.53	16.83 ± 4.77	$0.063^{+0.024}_{-0.021}$	< 26.03	0.45 ± 0.04
1522272275	219.0635	0.8046	6.6073	43.32 ± 0.02	325.20 ± 20.33	32.84	16.97 ± 3.57	$0.063^{+0.019}_{-0.017}$	26.29 ± 0.08	0.80 ± 0.07

Begley et al. (2024) discuss that their $f_{esc}^{Ly\alpha}$ - EW$_0$ relation agrees well with the relation derived for low-redshift LAEs (Sobral & Matthee 2019). The observed scatter in this relation are found to be well-consistent with that observed in both low and high-z LAE samples (see, Pucha et al. 2022; Roy et al. 2023). A similar positive correlation has also been observed in LAEs in the reionisation era (Saxena et al. 2024; Tang et al. 2024b). However, the slope, normalisation, and scatter of the observed $f_{esc}^{Ly\alpha}$ - EW$_0$ relationship are likely influenced by dust attenuation, differential dust geometry and ξ_{ion} (Matthee et al. 2017a; Harikane et al. 2018; Shivaei et al. 2018; Sobral & Matthee 2019). Additionally, for a given EW$_0$ value, intrinsic scatter in $f_{esc}^{Ly\alpha}$ is expected due to variations in stellar populations and dust/gas properties (Begley et al. 2024). We conclude that, despite the complexity of factors, $f_{esc}^{Ly\alpha}$ can be predicted within $\sim$0.5 dex of actual values from the $f_{esc}^{Ly\alpha}$ - EW$_0$ relation of Begley et al. (2024) using only the equivalent width information.

4. Results and discussions

We present photometric and spectroscopic properties (see Tables 1 and 2, respectively) of 22 LAEs at $5.5 \lesssim z \lesssim 6.6$. These sources have Ly$\alpha$ luminosities $\log(L_{Ly\alpha} \,[\mathrm{erg\,s^{-1}}]) = 42.4 - 43.5$ and Lyα rest-frame equivalent widths EW$_0 \simeq 10 - 72$ Å. In the following subsections, we explore the relation between the Lyα line width

and Lyα luminosity and investigate this relation in the context of the size of the ionised bubbles created by each LAE at the end of the reionisation era.

4.1 Evolution of the Lyα line width

We fit the Lyα lines with an asymmetric/skewed Gaussian. This provides excellent representation of all the Lyα profiles. All of the asymmetry parameters are positive, corresponding to red-skewed profiles. The asymmetry of all the lines also confirm that these are Lyα emission from star-forming galaxies rather than other emission lines from low-redshift interlopers. In Fig. 2, we present the evolution of Lyα line widths with Lyα luminosities across two redshifts ranges. For MAGPI LAEs, we find that at $z < 6$ (see Fig. 3, left panel), FWHM distribution is almost uniform, with no significant evolution with increasing luminosities. In contrast, $z > 6$ LAEs show a strong evolution of increasing line width with increasing luminosities (see Fig. 2, right panel). For comparison, we also include data from MUSE DEEP and MUSE WIDE surveys (Kerutt et al. 2022), bright LAEs from Shibuya et al. (2018), $z \sim 6.9$ LAEs from LAGER survey (Hu et al. 2017) and recent large sample of LAEs from Songaila et al. (2024), which allows a better understanding of the evolution of line widths across a wide redshift range ($5.5 \lesssim z \lesssim 7$) at the edge of reionisation. We note large uncertainties in luminosities and FWHMs
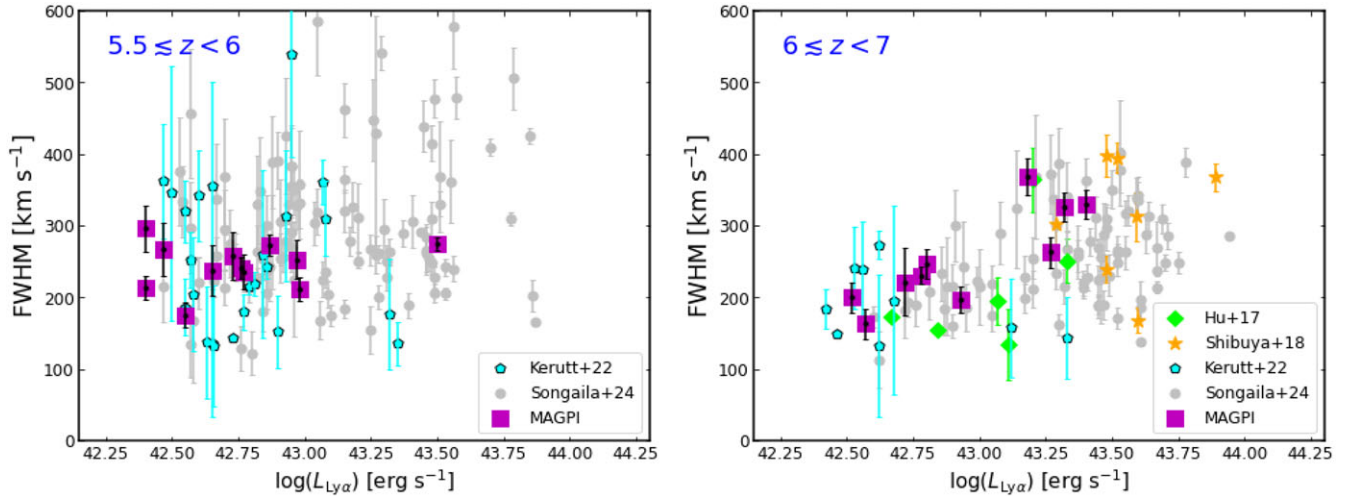
Figure 2. Evolution of Lyα line width is shown as function of Lyα luminosity at $5.5 \lesssim z < 6$ (left panel) and at $6 \lesssim z \lesssim 7$ (right panel). MAGPI LAEs (this work) are shown as purple squares. We also include data from MUSE DEEP and MUSE WIDE surveys (blue pentagons; Kerutt et al. 2022), (grey circles; Songaila et al. 2024), LAGER survey (green diamonds; Hu et al. 2017) and (orange stars; Shibuya et al. 2018).
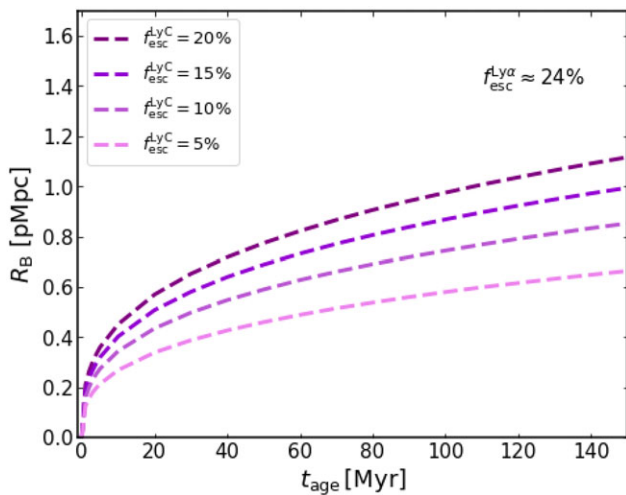
Figure 3. Radius of spherical bubble ionised by MAGPI2310222098 as a function of the age parameter (t_{age}), for different values of the LyC escape fraction ($f_{\mathrm{esc}}^{\mathrm{LyC}}$ = 5%, 10%, 15% and 20%). Here we assume a fixed Lyα escape fraction $f_{\mathrm{esc}}^{\mathrm{Lyα}} = 24\%$, as estimated (see Table 2).

in the data of Kerutt et al. (2022). Apart from that, we find our result is well-consistent with the others. We note that, at $z > 6$, line widths of MAGPI LAEs are narrower (FWHM $\lesssim 250\,\mathrm{km\,s^{-1}}$) at luminosities $\log(L_{\mathrm{Lyα}}\,[\mathrm{erg\,s^{-1}}]) < 43$, as compared to LAEs at $\log(L_{\mathrm{Lyα}}\,[\mathrm{erg\,s^{-1}}]) > 43$, where we find broader line widths (i.e. FWHM $> 260\,\mathrm{km\,s^{-1}}$). The visibility of Lyα emission from high-redshift star-forming galaxies is primarily determined by the star formation rate and ionising photon budget, which influence the size of ionised bubbles around them that allow Lyα photons to travel unattenuated along the line of sight (Malhotra & Rhoads 2006). Despite the fact that increasingly neutral IGM potentially scatters most of the Lyα photons and make the line narrower, the broadening of the line at $z > 6$ suggests that the high-luminosity LAEs may preferentially lie in more highly ionised regions than

the lower luminosity LAEs (Matthee et al. 2017b; Songaila et al. 2024), protecting themselves from the scattering effects of the IGM. In the next section, we discuss how LAEs themselves can produce ionised bubbles around them.

4.2 Ionising photon escape and size of ionised region

The absorption of ionising photons by the interstellar medium within galaxies leads to Lyα emissions through recombination processes, while photons that escape contribute to cosmic reionisation. The size of the ionised region (H II bubble) around an ionising source can be estimated by solving the evolution equation of the ionising front (e.g. Cen & Haiman 2000; Yajima, Sugimura, & Hasegawa 2018):

$$\frac{\mathrm{d}R_{\mathrm{B}}^3}{\mathrm{d}t} = 3\,H(z)\,R_{\mathrm{B}}^3 + \frac{3\,Q_{\mathrm{ion}}\,f_{\mathrm{esc}}^{\mathrm{LyC}}}{4\pi\,n_{\mathrm{H}}(z)} - C_{\mathrm{HII}}\,n_{\mathrm{H}}(z)\,\alpha_{\mathrm{rec}}\,R_{\mathrm{B}}^3 \qquad (3)$$

where R_{B} is the proper physical radius of ionised bubble in physical Mpc (pMpc), $H\,(z)$ is the Hubble parameter, Q_{ion} is the intrinsic production rate of ionising photons (in $\mathrm{s^{-1}}$), C_{HII} is the clumping factor of ionised hydrogen and α_{rec} is the temperature-dependent total recombination rate coefficient under Case B approximation (T = 10^4 K, $n_e = 350\,\mathrm{cm^{-3}}$). The mean hydrogen density of the IGM (n_{H}) scales with redshift as follows: $n_{\mathrm{H}} \approx 8.5 \times 10^{-5} \left(\frac{1+z}{8}\right)^3\,\mathrm{cm^{-3}}$ (see, Mason & Gronke 2020; Meyer et al. 2021).

We can define ionising photon production rate (Q_{ion}) in terms of direct Lyα observables (see, Matthee et al. 2017b; Yajima et al. 2018; Sobral & Matthee 2019; Matthee et al. 2022):

$$Q_{\mathrm{ion}}\,[s^{-1}] = \frac{L_{\mathrm{Lyα}}}{c_{\mathrm{Hα}}\left(1 - f_{\mathrm{esc}}^{\mathrm{LyC}}\right) \times \left(8.7\,f_{\mathrm{esc}}^{\mathrm{Lyα}}\right)} \qquad (4)$$

where $c_{\mathrm{Hα}} = 1.36 \times 10^{-12}$ erg (under case B recombination; Kennicutt 1998; Schaerer 2003). Here, we assume negligible nebular attenuation (Naidu et al. 2022). A detailed discussion on the role of dust in the context of Lyα and LyC escape can be found in

Kakiichi & Gronke (2021). In Section 3.3, we estimated Lyα escape fractions (within $\simeq 0.5$ dex) using its linear dependence on EW$_0$. However, this relation can be influenced by dust attenuation and $\xi_{\rm ion}$, as discussed in Section 3.3. A prominent degeneracy between dust extinction and $\xi_{\rm ion}$ has been observed in Sobral & Matthee (2019), where higher dust extinction allows for a lower $\xi_{\rm ion}$ and vice versa. Current data restrict us from accurately estimating both $f_{\rm esc}^{\rm Ly\alpha}$ and $\xi_{\rm ion}$ as it requires dust-corrected Hα luminosity. Direct observations of Balmer decrements and high-excitation UV lines are necessary to further validate and confirm our results.

A correlation between Lyα and LyC escape fractions has been investigated in several observational studies and hydrodynamical simulations (Verhamme et al. 2017; Chisholm et al. 2018; Flury et al. 2022; Maji et al. 2022). Begley et al. (2024) find a linear dependence between $f_{\rm esc}^{\rm LyC}$ and $f_{\rm esc}^{\rm Ly\alpha}$. Using this relation, we estimate that our sources have $f_{\rm esc}^{\rm LyC} = 0.5 - 4\%$. Hydrodynamical and radiative transfer simulations are used to calibrate the same relation (Maji et al. 2022), using which we get $f_{\rm esc}^{\rm LyC} < 3\%$ for our sources. However, this correlation between Lyα and LyC escape does not seem to work well for LyC leakers at higher redshifts (see, Kerutt et al. 2024). Kinematics and ISM properties of high-redshift leakers are more complex (Guaita et al. 2015) as compared to low-redshift leakers. A spatial offset between Lyα and LyC emission has been observed in high-redshift leakers (Kerutt et al. 2024; Gupta et al. 2024), which indicates that the two are escaping from different locations in the galaxy. For instance, high-redshift leakers prefer asymmetric escape (indicating scattering or expanding gas) rather than through optically thin ionised channel, which seems to be the case for low-redshift leakers (Kerutt et al. 2024).

We do not expect LAEs in our sample to be strong LyC leakers. Hence, we simply assume a fiducial value of LyC escape $f_{\rm esc}^{\rm LyC} = 5\%$ for our sources throughout the analysis. The ionising photon production efficiency is defined as the ratio of $Q_{\rm ion}$ and intrinsic UV luminosity density ($L_{\rm UV,\nu}$) (Matthee et al. 2017b) :

$$\xi_{\rm ion} \ [{\rm Hz\ erg}^{-1}] = \frac{Q_{\rm ion}}{L_{\rm UV,\nu}} \tag{5}$$

We obtain $L_{\rm UV,\nu}$ from M$_{\rm UV}$, assuming negligible dust attenuation. We refer to Bouwens et al. (2016) for a discussion on the impact of dust attenuation on $\xi_{\rm ion}$. Our measured M$_{\rm UV}$ values (see Table 1) indicate that these LAEs are UV-bright ($-19.74 \leq$ M$_{\rm UV} \leq -23.27$). The estimated $\xi_{\rm ion}$ values are presented in Table 2. For the sources, which are detected in HSC, we find an average ionising photon production efficiency $\log(\xi_{\rm ion}\ [{\rm Hz\ erg}^{-1}]) = 25.51$ at $z < 6$, while $\log(\xi_{\rm ion}\ [{\rm Hz\ erg}^{-1}]) = 25.74$ at $z > 6$. The slight evolution of $\xi_{\rm ion}$ with redshift is consistent with the previous studies (eg. Bouwens et al. 2014; Endsley et al. 2021b; Simmonds et al. 2023; Tang et al. 2023; Saxena et al. 2024). This aligns with the idea that younger galaxies may achieve higher ionising photon production efficiencies. However, the evolution is very mild which could suggest that the production and escape of ionising photons are governed by physical processes operating on much shorter timescales, such as intense star formation or supernova activity, which do not show a strong trend with redshift (Saxena et al. 2024). Further, we also note that some of the low-equivalent width (therefore, low $f_{\rm esc}^{\rm Ly\alpha}$) LAEs (EW$_0 < 20$ Å; i.e, MAGPI1503111271, MAGPI1204117107, MAGPI1528094186, and MAGPI1522272275) show higher $\xi_{\rm ion}$ (see Table 2). Such a

tentative anti-correlation between $f_{\rm esc}^{\rm Ly\alpha}$ and $\xi_{\rm ion}$ has been reported in a large sample of LAEs from JEMS and MUSE (see Simmonds et al. 2023). This could indicate a time delay between production and escape of ionising photons in these galaxies (Katz et al. 2020), which again may be linked to supernova activity.

For constant Lyα luminosity and $f_{\rm esc}^{\rm LyC}$, hence for a constant production rate $Q_{\rm ion}$, Equation (3) can be solved analytically to obtain an expression of bubble sizes that can be produced by the LAE on its own. For instance, neglecting the accelerated expansion due to Hubble flow and for luminous sources at $z \lesssim 8$, when the recombination rate is relatively low, second term of Equation (3) dominates and we get an expression for bubble radius (Cen & Haiman 2000):

$$R_{\rm B} \approx \left(\frac{3\ Q_{\rm ion}\ f_{\rm esc}^{\rm LyC}\ t_{\rm age}}{4\pi\ n_{\rm H}(z)} \right)^{1/3} \tag{6}$$

where $t_{\rm age}$ is the time since the ionising source has switched on. For these estimates, we assume a fiducial value of $t_{\rm age} = 100$ Myr (a reasonable amount of time for $f_{\rm esc}^{\rm LyC} = 5\%$; see Witstok et al. 2024; Whitler et al. 2024) for all the LAEs. Recent studies note that the inferred bubble size does not strongly depend on small deviations in LyC escape fraction and age (see, Witstok et al. 2024; Torralba-Torregrosa et al. 2024). For one luminous LAE (ID: MAGPI2310222098), we study the evolution of bubble size as a function of $t_{\rm age}$ for different values of the LyC escape fraction (see, Fig. 3). For a constant Lyα escape fraction ($f_{\rm esc}^{\rm Ly\alpha} \approx 24\%$), we find that this LAE is capable of ionising a bubble of radius $R_{\rm B} \sim 0.59$ pMpc in $t_{\rm age} = 100$ Myr for a LyC escape of $f_{\rm esc}^{\rm LyC} = 5\%$ while it takes $t_{\rm age} = 50\ (30)$ Myr to ionise the same bubble size, when $f_{\rm esc}^{\rm LyC} = 10\ (15)\%$. We also note that $t_{\rm age}$ depends on the actual time duration of constant star-formation within the galaxy, which is fundamentally bounded to $\lesssim +200$ Myr at this epoch (see, Tacchella et al. 2018; Whitler et al. 2023).

Based on the assumptions mentioned above ($t_{\rm age} = 100$ Myr and $f_{\rm esc}^{\rm LyC} = 5\%$), we find that each of our LAEs reside in ionised bubbles of radii $R_{\rm B} = 0.31 - 0.86$ pMpc (see, Table 2). From Equations (4) and (6), we note that bubble radius scales with the Lyα luminosity as $R_{\rm B} \propto L_{\rm Ly\alpha}^{1/3}$. Modeling of Ly$\alpha$ emission and transmission during the EoR also predicts that Lyα luminosity increases with $R_{\rm B}$ due to higher IGM transmission for large ionised bubbles (see, Yajima et al. 2018). We find a linear correlation between bubble radii and Lyα line widths (see Fig. 4) with high statistical significance (Spearman correlation coefficient $= 0.53$ and p-value $= 0.006$). This trend is more prominent in LAEs at $z > 6$, which is expected given the correlation between Lyα luminosity and line width at $z > 6$, as discussed in the previous section. This again supports the fact that broadening of Lyα lines at $z > 6$ is due to large ionised bubble which are created around them, allowing most of the Lyα photons to come out of that the galaxy without suffering from much scattering in the IGM (Songaila et al. 2022; Songaila et al. 2024).

At high redshifts, Lyα lines are usually redshifted with respect to systemic velocity due to strong outflows, which facilitates the transmission of Lyα photons through IGM (Dijkstra, Mesinger, & Wyithe 2011). The velocity offset of the red peak has been used to place lower limits on the bubble sizes required for IGM transmission (Mason & Gronke 2020; Witstok et al. 2024). Considering a patchy reionisation scenario, where a galaxy is typically surrounded by a completely neutral IGM, it is found that Lyα can
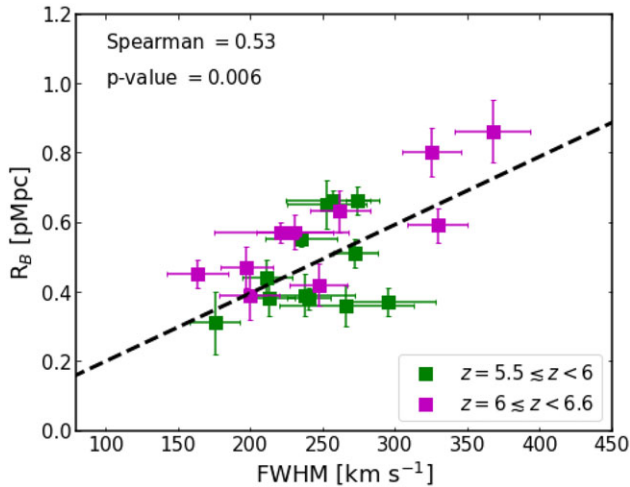
Figure 4. Evolution of the bubble radius as a function of Lyα line width for our 22 MAGPI LAEs. LAEs at $5.5 \lesssim z < 6$ are highlighted in green squares whereas LAEs at $z > 6$ are shown in purple squares. Significance of the plot (Spearman correlation coefficient and p-value) are shown in the top left corner.

be detected at a high velocity offset of $\gtrsim +300$ km s^{-1} when the galaxy is situated in a ionised region of radius $R_B \gtrsim 0.1$ pMpc (see Mason & Gronke 2020; Umeda et al. 2023). A Bayesian approach of modeling intrinsic Lyα profiles has predicted the size of ionised regions to be $R_B = 0.5 - 2.5$ pMpc at $z > 6$ (Hayes & Scarlata 2023). Witstok et al. (2024) find that LAEs with relatively low Lyα velocity offset ($\lesssim +300$ km s^{-1}) with moderately high escape fraction can represent ionised regions of sizes $R_B = 0.1 - 1$ pMpc. Further, several attempts have been made to put constraints on the size of ionised regions that allow blue peak of Lyα to be detected at $z > 6$, where it is found that the blue peak can be detected if the source galaxy resides in a highly ionised region ($x_{HI} > 10^{-5}$) of radius $R_B \gtrsim 0.5$ pMpc (see, Mason & Gronke 2020; Torralba-Torregrosa et al. 2024). We note that, while some of our LAEs show larger bubble sizes, we cannot always anticipate seeing a blue-peak emission from them, as these photons might be heavily absorbed by neutral hydrogen in the circumgalactic medium (CGM; Henry et al. 2015; Gazagnes et al. 2020; Endsley & Stark 2022).

Lyα radiative transfer modeling suggests strong correlation between Lyα velocity offset and N_{HI} (Verhamme et al. 2015). As N_{HI} increases the peak velocity shifts farther from the systemic velocity. Further, shell model predicts that for a low N_{HI} and high outflow velocity, most of the Lyα photons can directly escape at the line centre frequency (Yajima et al. 2018). In addition, line width becomes narrower when N_{HI} decreases. This is expected as low N_{HI} shifts the peak to shorter wavelengths, where Lyα flux is significantly reduced due to IGM scattering. While IGM radiative transfer establishes a typical correlation between the line width and velocity offset of Lyα red peaks (e.g. Neufeld 1990; Verhamme et al. 2018; Li & Gronke 2022), this trend is expected to change at high redshifts due to IGM absorption. Ignoring such complicated radiative transfer effects at high redshifts, we can simply assume that Lyα line width is positively correlated with N_{HI} as FWHM $\simeq 320 \left(\frac{N_{HI}}{10^{20} \text{cm}^{-2}} \right)^{1/3}$ (Dijkstra 2017; Li & Gronke 2022) for a static shell with temperature $T_{eff} = 10^4$ K. This translates to a column density $\log(N_{HI}) \sim 20.18$ cm^{-2} for the highest FWHM LAE in our

sample (i.e. MAGPI1204117107 at $z = 6.046$). Further, using the correlation between velocity offset and $\log(N_{HI})$ (which is approximated by a second order polynomial, see Fig. 2 of Verhamme et al. 2015), we expect this line to be at an offset of 300 km s^{-1}. We follow the IGM transmission model of Witstok et al. (2024) and find that this LAE can have >30% IGM transmission if it resides inside a bubble of radius $R_B = 0.86$ pMpc. This estimation is in agreement with the findings of Endsley et al. (2022), where they discover boosted Lyα transmission in LAEs with large velocity offsets and broad line widths. On the other hand, MAGPI2310245276 at $z = 6.039$ (FWHM $= 199.64$ km s^{-1}) can only transmit <10% of Lyα photons if it resides in $R_B = 0.39$ pMpc bubble. However, it is also possible that for a very low velocity offset ($< +200$ km s^{-1}), a sufficiently large ($R_B > 1.5$ pMpc) bubble will be able to transmit $> +60\%$ of Lyα photons (see, Fig. 3 of Witstok et al. 2024) by reducing the scattering effect, which can increase the observed Lyα luminosity and may allow some photons to escape on the bluer side. A better understanding of N_{HI} – FWHM – velocity offset relation at $z > 6$ will require efficient radiative transfer modeling of these high-redshift LAEs.

Our analysis suggests that galaxies with broader Lyα emission lines are generally located within larger ionised bubbles. However, we caution that this may not always hold true. For instance, UV-bright galaxies in the reionisation era may exhibit wider Lyα line profiles if they have more H I present in their CGM, resulting in more scattering of Lyα photons (see, Tang et al. 2023). Moreover, UV-bright galaxies are found to display larger Lyα velocity offsets (e.g. Endsley et al. 2022; Valentino et al. 2022; Tang et al. 2023; Witten et al. 2023). In such cases, most of the Lyα photons emerge at relatively high velocities, experiencing minimal attenuation by the neutral IGM (see, Mason & Gronke 2020). Visibility of Lyα during reionisation can also be enhanced by efficient ionising photon production due to hard ionising field (e.g. Mainali et al. 2018; Tang et al. 2023), or if Lyα is produced in gas clumps moving with large peculiar motions, leading to intrinsically broad Lyα profile (e.g. Endsley et al. 2022). Therefore, wide Lyα lines from LAEs can survive even in moderate-sized ionised bubbles (e.g. Endsley et al. 2022). Future observations of Lyα in both UV-bright and faint galaxies during the reionisation era will provide more precise constraints on bubble sizes and the influence of the IGM on Lyα transmission.

4.3 Closely separated LAE pair: Overlapping bubbles?

We find two closely separated LAE pairs. There are two LAEs in MAGPI2310 field (MAGPI IDs: 2310245276 and 2310222098) at $z = 6.039$ and $z = 6.1485$, respectively, are located 36″ apart on the sky, which corresponds to a physical distance of 203 kpc. Their separation along the line of sight is 6.32 pMpc. As a result, the estimated radii of their bubbles indicate that these bubbles do not overlap. We also find two LAEs at $z = 6.046$ in MAGPI1529 field (MAGPI IDs: 1529106057 and 1529110045), whose redshifts differ only by 0.0002, which corresponds to a velocity shift of only 61 km s^{-1}. They are located only 3″ apart on the sky (see Fig. 5), translating to a projected physical separation of 15.92 kpc. The estimated bubble radii for them suggest that their bubbles overlap and they likely sit inside a single large ionised region (see Fig. 5, right panel).

Closely separated LAEs have been previously observed in the reionisation era (see, Castellano et al. 2016; Hu et al. 2017; Tilvi et al. 2020; Endsley et al. 2021a; Endsley & Stark 2022;
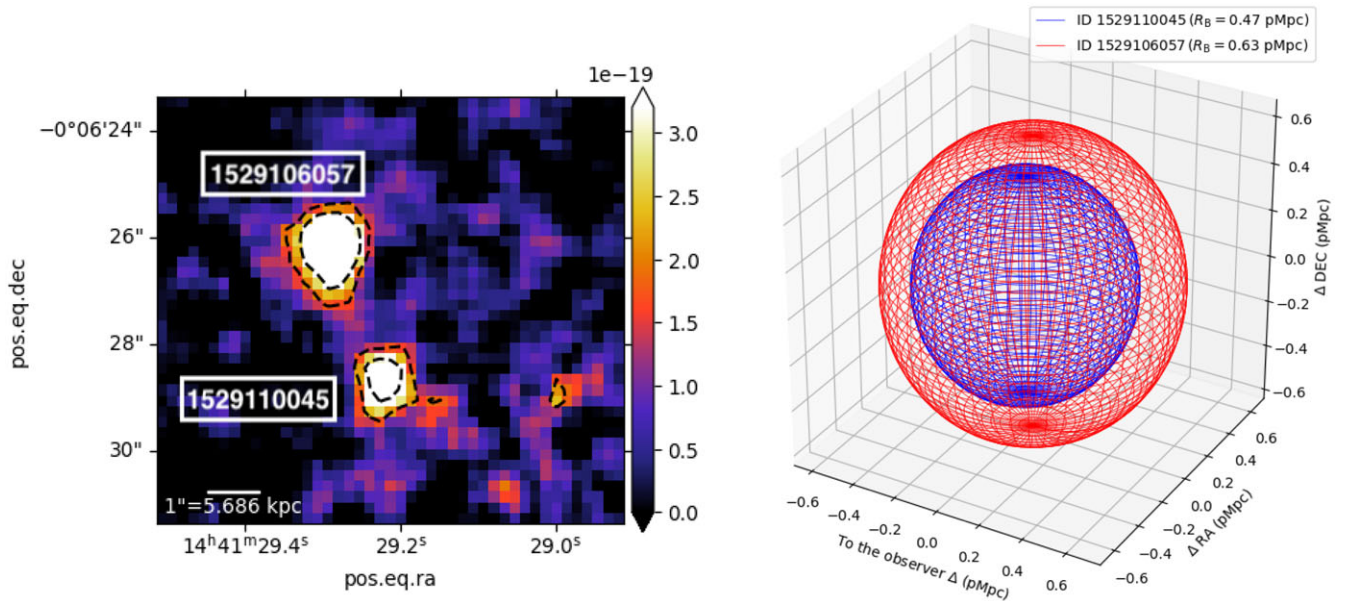
Figure 5. *Left panel:* Synthetic MUSE Lyα narrow band (NB) image collapsed for wavelengths within 8 550–8 590 Å, showing two LAEs with MAGPI IDs 1529106057 and 1529110045 at $z = 6.046$, separated by a physical distance of 15.92 kpc. Contours are shown as black dashed lines at the 2 and 4σ significance levels. *Right panel:* Three-dimensional visualisation of the size of ionised bubbles created by them along the line of sight. Bubbles are shown in wire-frame spheres centred on each LAE. The centre of the LAE MAGPI1529110045 is at the origin of this 3D plot.

Chen et al. 2024; Witstok et al. 2024). Many of these LAEs are found to reside in overdense regions populated by fainter galaxies (e.g. Castellano et al. 2016; Castellano et al. 2018; Chen et al. 2024; Witstok et al. 2024; Whitler et al. 2024). On the other hand, Endsley & Stark (2022) detect many UV-bright galaxies making an overdense region around three closely separated Lyman-break galaxies at $z \sim 6.8$. Closely separated LAEs in overdense regions can cause bubble overlap, which results in the formation of giant ionised bubbles, allowing a boosted transmission of Lyα through the neutral IGM (Mason et al. 2018; Jung et al. 2022a). With our current data, we cannot yet fully characterise the extent of the ionised regions surrounding the closely separated LAEs in our sample. Future spectroscopic follow-up of these LAEs, as well as spectroscopy and deep photometry focusing on fainter galaxies in the surrounding area are necessary to place further constraints on the size of the ionised bubbles in those regions. Further, we note that our LAE pair at $z = 6.046$ is UV-bright ($M_{UV} \sim -21$), similar to that of the closely separated LAEs discussed in Endsley et al. (2021a), potentially indicating that UV-bright galaxies in overdense regions enhance Lyα transmission (Endsley et al. 2021a; Endsley & Stark 2022). Reionisation simulation has also predicted that reionisation is more advanced in high-density regions compared to those that are isolated, indicating that LAE clustering could lead to Lyα emission that is less-attenuated by the IGM (Qin et al. 2022; Lu et al. 2024). Considering different models for the internal velocity structure of a galaxy (i.e. expanding shell or cloud), Yajima et al. (2018) find that the overlapping bubbles are likely to affect the outflow velocity. Further, LAE clustering during reionisation supports an accelerated reionisation scenario, suggesting that reionisation proceeds faster in regions around such galaxies (see, Endsley et al. 2021a).

5. Summary and conclusions

We present spectroscopic properties of 22 newly discovered LAEs at the edge of reionisation era ($5.5 \lesssim z \lesssim 6.6$), identified in the MAGPI data. For 17 of them covered in the HSC-Subaru Wide layer, we provide photometric magnitudes and 2σ limits (for non-detections) of i, z, y broad-band filters. The HSC-y band magnitudes indicate that our LAEs are UV-bright, with rest-frame absolute UV magnitudes $-19.74 \leq M_{UV} \leq -23.27$. We summarise our main findings as follows:

(i) We observe that for $z < 6$, the FWHM distribution of LAEs remains almost uniform with no significant change as luminosity increases. However, for $z > 6$, there is a noticeable increase in line width with increasing luminosity. This broadening at high redshifts suggests that high-luminosity LAEs at $z > 6$ may be located in more highly ionised regions of the IGM, despite the fact that a more neutral IGM would typically narrow the line by scattering more Lyα photons.

(ii) We also find that some low-equivalent width (EW$_0 < 20$ Å) LAEs exhibit higher ionising photon production efficiency. This suggests a possible anti-correlation between the Lyα escape fraction and ξ_{ion}, as observed in other studies. This anti-correlation might indicate a time delay between the production and escape of ionising photons in these galaxies, potentially related to supernova activity.

(iii) Using the Lyα spectroscopic properties and based on some assumptions, we find that LAEs in our sample can ionise bubbles of size $R_B = 0.31 - 0.86$ pMpc. The study also finds a significant linear correlation between bubble radii and Lyα line widths. The correlation is particularly strong

in LAEs at $z > 6$, supporting the idea that the broadening of Lyα lines at these high redshifts is due to large ionised bubbles around those galaxies. Larger bubbles allow most of the Lyα photons to escape the galaxy with minimal scattering in the IGM. Based on simple model and assumptions, Lyα line width can be used to constrain the IGM transmission as well as bubble sizes. A narrow line width could indicate low H I column density, which will force Lyα photons to escape close to the line centre, where line flux is significantly reduced due to IGM scattering. However, this can be uncertain and depends on the complex radiative transfer of Lyα photons in the IGM and CGM. We also discuss that the enhanced visibility of Lyα could also be due to several other factors such as large velocity offset of Lyα form systemic velocity, hardness of ionising field and due to large peculiar motions of gas clumps present in the galaxy. In such cases, wide Lyα can transmit through the neutral IGM even when the ionised bubble size is small.

(iv) Two closely separated LAE pairs are discovered in two MAGPI fields. One pair at $z = 6.046$ is just $3''$ apart on the sky, which corresponds to a physical separation of about 15.92 kpc. Their bubble radii indicate that they sit inside a single large ionised region. As far as we know, this is the pair of LAEs with the smallest separation ever identified in the reionisation era. Such overlap of ionised bubbles due to clustering of LAEs during reionisation increases the size of the ionised regions and enhances the transmission of Lyα through the neutral IGM. Future spectroscopic and photometric follow-up of the area surrounding these LAEs will detect fainter galaxies, allowing for improved constraints on the size of the ionised bubbles in those regions.

This study shows how wide-area Lyα spectroscopy across a broad range of redshifts can aid in identifying and characterising ionised bubbles formed during reionisation. In the future, as new reionisation-era LAEs will be discovered in the upcoming MAGPI fields, it will be possible to place more precise constraints on the evolution of line width with luminosity. Additionally, spectroscopic follow-up using infrared spectroscopy will allow for the measurement of systemic redshifts, leading to more accurate determinations of bubble sizes.

References

Aihara, H., et al. 2018, PASJ, 70, S4

Aihara, H., et al. 2019, PASJ, 71, 114

Bacon, R., et al. 2010, in Society of Photo-Optical Instrumentation Engineers (SPIE) Conference Series, Vol. 7735, Ground-based and Airborne Instrumentation for Astronomy III, ed. I. S. McLean, S. K. Ramsay, & H. Takami, 773508

Bacon, R., et al. 2023, A&A, 670, A4

Bagley, M. B., et al. 2017, ApJ, 837, 11

Becker, G. D., et al. 2015, MNRAS, 447, 3402

Begley, R., et al. 2024, MNRAS, 527, 4040

Bosman, S. E. I., et al. 2022, MNRAS, 514, 55

Bouwens, R. J., et al. 2016, ApJ, 831, 176

Bouwens, R. J., et al. 2014, ApJ, 793, 115

Bruzual, G., & Charlot, S. 2003, MNRAS, 344, 1000

Cain, C., D'Aloisio, A., Gangolli, N., & Becker, G. D. 2021, ApJ, 917, L37

Castellano, M., et al. 2016, ApJ, 818, L3

Castellano, M., et al. 2018, ApJ, 863, L3

Cen, R., & Haiman, Z. 2000, ApJ, 542, L75

Chen, Z., et al. 2024, MNRAS, 528, 7052

Chisholm, J., et al. 2018, A&A, 616, A30

Choustikov, N., et al. 2024, MNRAS, 529, 3751

Claeyssens, A., et al. 2019, MNRAS, 489, 5022

Dayal, P., et al. 2020, MNRAS, 495, 3065

Dijkstra, M. 2017, arXiv e-prints, arXiv:1704.03416

Dijkstra, M., Mesinger, A., & Wyithe, J. S. B. 2011, MNRAS, 414, 2139

Driver, S. P., et al. 2011, MNRAS, 413, 971

Dunlop, J. S., et al. 2013, MNRAS, 432, 3520

Endsley, R., & Stark, D. P. 2022, MNRAS, 511, 6042

Endsley, R., et al. 2021a, MNRAS, 502, 6044

Endsley, R., Stark, D. P., Chevallard, J., & Charlot, S. 2021b, MNRAS, 500, 5229

Endsley, R., et al. 2022, MNRAS, 517, 5642

Fan, X., et al. 2006, AJ, 132, 117

Finkelstein, S. L., et al. 2019, ApJ, 879, 36

Flury, S. R., et al. 2022, ApJ, 930, 126

Foster, C., et al. 2021, PASA, 38, e031

Furtak, L. J., et al. 2022, MNRAS, 516, 1373

Gazagnes, S., Chisholm, J., Schaerer, D., Verhamme, A., & Izotov, Y. 2020, A&A, 639, A85

Graham, A. W., & Driver, S. P. 2005, PASA, 22, 118

Guaita, L., et al. 2015, A&A, 576, A51

Gupta, A., et al. 2024, ApJ, 973, 169

Harikane, Y., et al. 2018, ApJ, 859, 84

Hashimoto, T., et al. 2017, A&A, 608, A10

Hayes, M. J., Runnholm, A., Gronke, M., & Scarlata, C. 2021, ApJ, 908, 36

Hayes, M. J., & Scarlata, C. 2023, ApJ, 954, L14

Henry, A., Scarlata, C., Martin, C. L., & Erb, D. 2015, ApJ, 809, 19

Herenz, E. C., & Wisotzki, L. 2017, A&A, 602, A111

Herenz, E. C., et al. 2017, A&A, 606, A12

Hinton, S. R., Davis, T. M., Lidman, C., Glazebrook, K., & Lewis, G. F. 2016, A&C, 15, 61

Hoag, A., et al. 2019, ApJ, 878, 12

Hu, E. M., et al. 2010, ApJ, 725, 394

Hu, E. M., et al. 2016, ApJ, 825, L7

Hu, W., et al. 2017, ApJ, 845, L16

Inoue, A. K., Shimizu, I., Iwata, I., & Tanaka, M. 2014, MNRAS, 442, 1805

Izotov, Y. I., et al. 2020, MNRAS, 491, 468

Izotov, Y. I., et al. 2018, MNRAS, 478, 4851

Jones, G. C., et al. 2024, arXiv e-prints, arXiv:2409.06405

Jung, I., et al. 2022a, ApJ, 933, 87

Jung, I., et al. 2022b, arXiv e-prints, arXiv:2212.09850

Jung, I., et al. 2024, ApJ, 967, 73

Kakiichi, K., Dijkstra, M., Ciardi, B., & Graziani, L. 2016, MNRAS, 463, 4019

Kakiichi, K., & Gronke, M. 2021, ApJ, 908, 30

Katz, H., et al. 2020, MNRAS, 498, 164

Katz, H., et al. 2022, MNRAS, 515, 4265

Kennicutt Jr., R. C. 1998, ARA&A, 36, 189

Kerutt, J., et al. 2022, A&A, 659, A183

Kerutt, J., et al. 2024, A&A, 684, A42

Konno, A., et al. 2014, ApJ, 797, 16

Konno, A., et al. 2018, PASJ, 70, S16

Kulkarni, G., et al. 2019, MNRAS, 485, L24

Laursen, P., Sommer-Larsen, J., Milvang-Jensen, B., Fynbo, J. P. U., & Razoumov, A. O. 2019, A&A, 627, A84

Li, Z., & Gronke, M. 2022, MNRAS, 513, 5034

Lin, X., et al. 2024, ApJS, 272, 33

Lu, T.-Y., et al. 2024, MNRAS, 528, 4872

Mainali, R., et al. 2018, MNRAS, 479, 1180

Maji, M., et al. 2022, A&A, 663, A66

Malhotra, S., & Rhoads, J. E. 2006, ApJ, 647, L95

Mascia, S., et al. 2023, A&A, 672, A155

Maseda, M. V., et al. 2020, MNRAS, 493, 5120

Mason, C. A., & Gronke, M. 2020, MNRAS, 499, 1395

Mason, C. A., et al. 2018, ApJ, 857, L11

Matthee, J., et al. 2017a, MNRAS, 465, 3637

Matthee, J., et al. 2017b, MNRAS, 472, 772

Matthee, J., et al. 2015, MNRAS, 451, 400

Matthee, J., et al. 2022, MNRAS, 512, 5960

Meyer, R. A., Laporte, N., Ellis, R. S., Verhamme, A., & Garel, T. 2021, MNRAS, 500, 558

Miyazaki, S., et al. 2018, PASJ, 70, S1

Mukherjee, T., et al. 2023, A&A, 680, L5

Naidu, R. P., et al. 2020, ApJ, 892, 109

Naidu, R. P., et al. 2022, MNRAS, 510, 4582

Nakajima, K., Ellis, R. S., Robertson, B. E., Tang, M., & Stark, D. P. 2020, ApJ, 889, 161

Nakane, M., et al. 2024, ApJ, 967, 28

Napolitano, L., et al. 2024, A&A, 688, A106

Neufeld, D. A. 1990, ApJ, 350, 216

Ning, Y., et al. 2023, ApJ, 944, L1

Pentericci, L., et al. 2011, ApJ, 743, 132

Pentericci, L., et al. 2014, ApJ, 793, 113

Prieto-Lyon, G., et al. 2023, A&A, 672, A186

Pucha, R., et al. 2022, AJ, 164, 159

Qin, Y., et al. 2022, MNRAS, 510, 3858

Robertson, B. E., Ellis, R. S., Dunlop, J. S., McLure, R. J., & Stark, D. P. 2010, Natur, 468, 49

Robertson, B. E., Ellis, R. S., Furlanetto, S. R., & Dunlop, J. S. 2015, ApJ, 802, L19

Roy, N., et al. 2023, ApJ, 952, L14

Santos, S., Sobral, D., & Matthee, J. 2016, MNRAS, 463, 1678

Saxena, A., et al. 2024, A&A, 684, A84

Schaerer, D. 2003, A&A, 397, 527

Schaerer, D., et al. 2022, A&A, 658, L11

Shibuya, T., et al. 2014, ApJ, 788, 74

Shibuya, T., et al. 2018, PASJ, 70, S15

Shivaei, I., et al. 2018, ApJ, 855, 42

Simmonds, C., et al. 2023, MNRAS, 523, 5468

Smith, A., et al. 2022, MNRAS, 512, 3243

Sobral, D., & Matthee, J. 2019, A&A, 623, A157

Songaila, A., Barger, A. J., Cowie, L. L., Hu, E. M., & Taylor, A. J. 2022, ApJ, 935, 52

Songaila, A., Cowie, L. L., Barger, A. J., Hu, E. M., & Taylor, A. J. 2024, arXiv e-prints, arXiv:2407.08772

Songaila, A., et al. 2018, ApJ, 859, 91

Stark, D. P., et al. 2017, MNRAS, 464, 469

Steidel, C. C., et al. 2018, ApJ, 869, 123

Tacchella, S., Bose, S., Conroy, C., Eisenstein, D. J., & Johnson, B. D. 2018, ApJ, 868, 92

Tang, M., Stark, D. P., Topping, M. W., Mason, C., & Ellis, R. S. 2024a, arXiv e-prints, arXiv:2408.01507

Tang, M., et al. 2023, MNRAS, 526, 1657

Tang, M., et al. 2024b, MNRAS, 531, 2701

Taylor, A. J., Barger, A. J., Cowie, L. L., Hu, E. M., & Songaila, A. 2020, ApJ, 895, 132

Taylor, A. J., Cowie, L. L., Barger, A. J., Hu, E. M., & Songaila, A. 2021, ApJ, 914, 79

Tilvi, V., et al. 2014, ApJ, 794, 5

Tilvi, V., et al. 2020, ApJ, 891, L10

Torralba-Torregrosa, A., et al. 2024, arXiv e-prints, arXiv:2404.10040

Umeda, H., et al. 2023, arXiv e-prints, arXiv:2306.00487

Urrutia, T., et al. 2019, A&A, 624, A141

Valentino, F., et al. 2022, ApJ, 929, L9

Verhamme, A., Orlitová, I., Schaerer, D., & Hayes, M. 2015, A&A, 578, A7

Verhamme, A., et al. 2017, A&A, 597, A13

Verhamme, A., et al. 2018, MNRAS, 478, L60

Weilbacher, P. M., et al. 2020, A&A, 641, A28

Weinberger, L. H., Kulkarni, G., Haehnelt, M. G., Choudhury, T. R., & Puchwein, E. 2018, MNRAS, 479, 2564

Whitler, L., et al. 2023, MNRAS, 519, 157

Whitler, L., et al. 2024, MNRAS, 529, 855

Whitler, L. R., et al. 2020, MNRAS, 495, 3602

Witstok, J., et al. 2024, A&A, 682, A40

Witten, C., et al. 2024, NatAs, 8, 384

Witten, C. E. C., Laporte, N., & Katz, H. 2023, ApJ, 944, 61

Xu, X., et al. 2022, ApJ, 933, 202

Yajima, H., Sugimura, K., & Hasegawa, K. 2018, MNRAS, 477, 5406

Yang, H., et al. 2017, ApJ, 844, 171

Appendix 1. Fitting Lyα lines
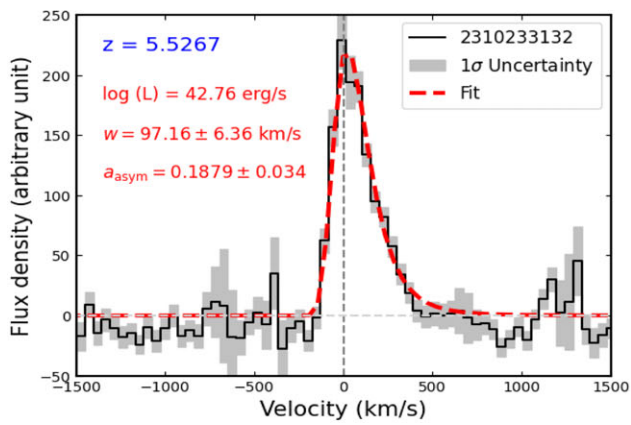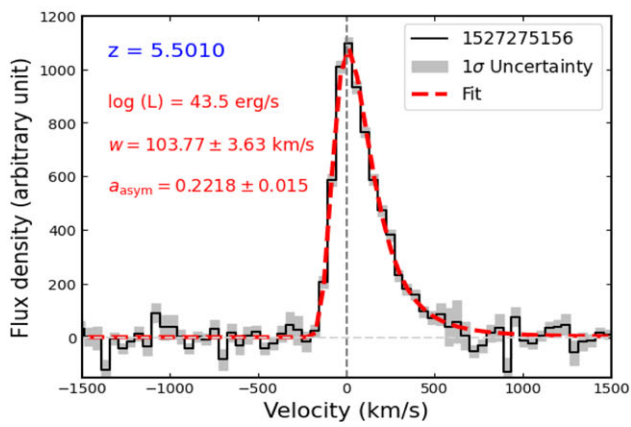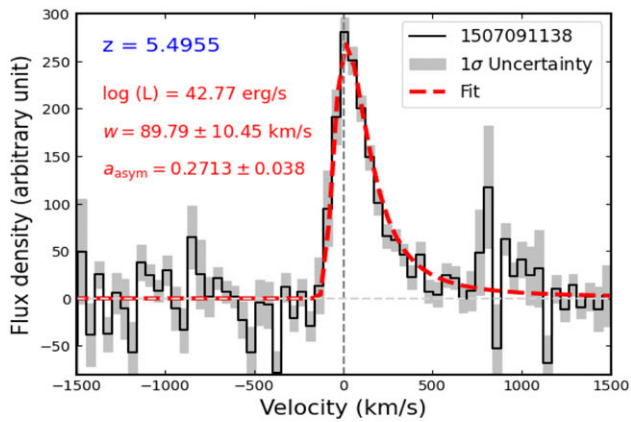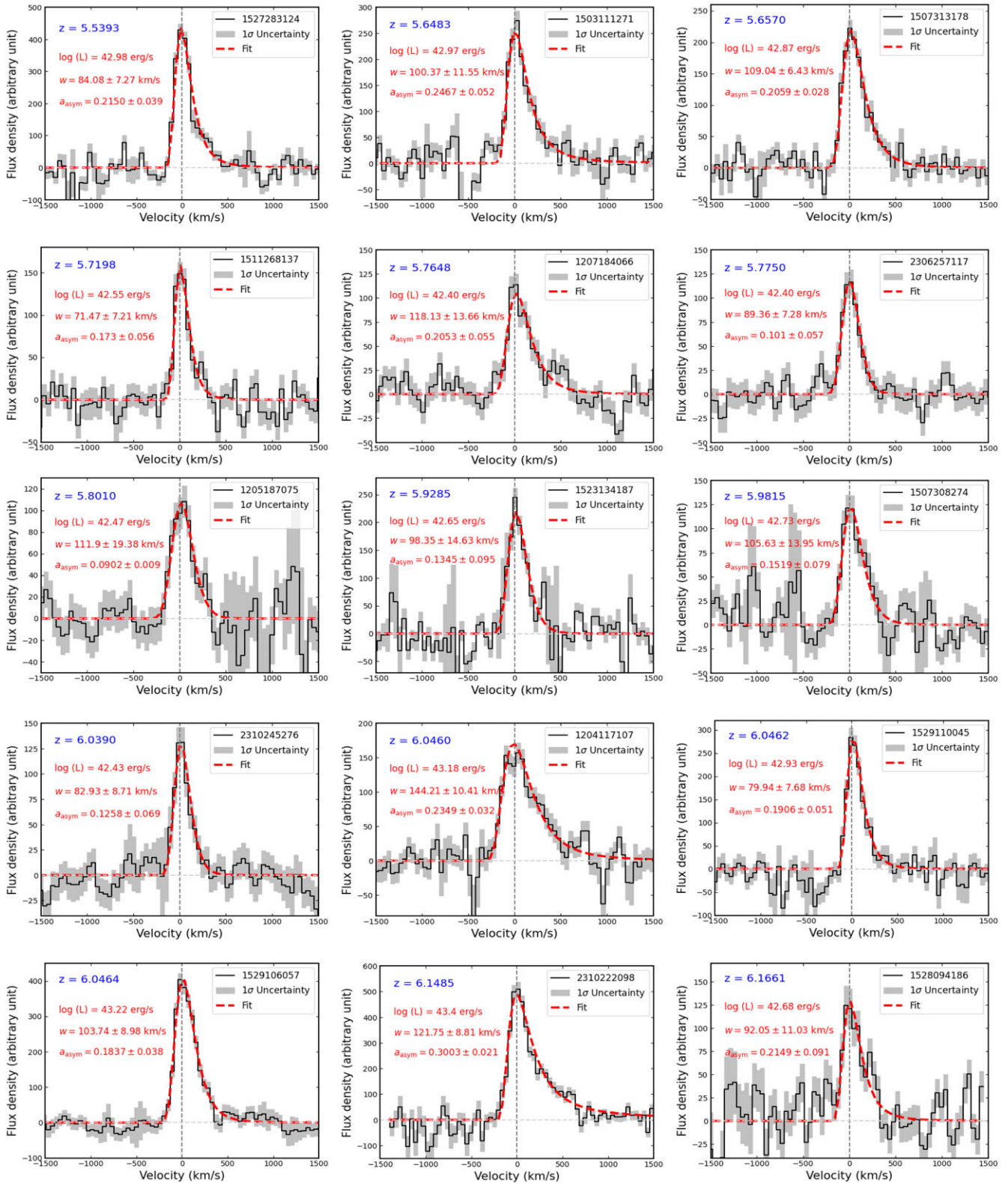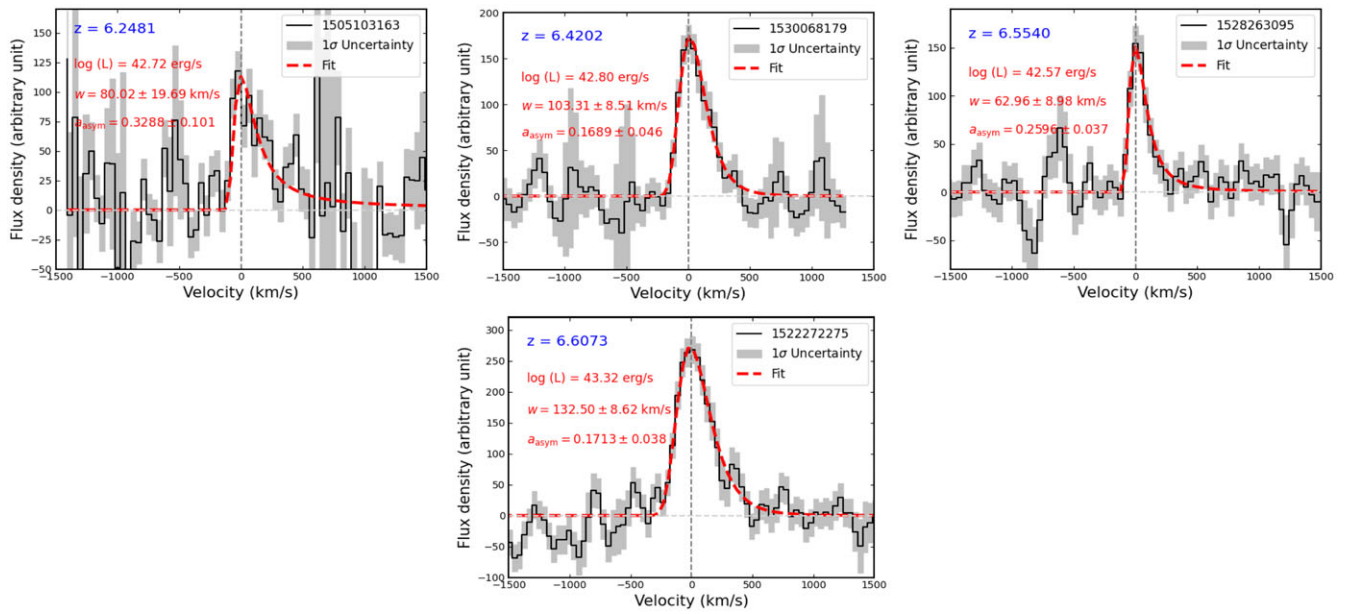
Figure A1. Shown are the velocity profiles of 22 LAEs at $5.5 \lesssim z \lesssim 6.6$. 1D spectrum (solid black, named by corresponding MAGPI ID) and associated $\pm 1\sigma$ uncertainty on the flux density (grey shaded), along with the asymmetric Gaussian fit (dashed-red) to the spectrum for each LAE are presented in each panels. In each panel, luminosity, redshift and best-fit parameters such as w defining FWHM, and asymmetry parameter are given in the left corners.